Materials Science Forum
ISSN: 1662-9752, Vol. 1183, pp 93-105
doi:10.4028/p-K6OYoi

Submitted: 2026-01-20
Revised: 2026-02-17
Accepted: 2026-02-25
Online: 2026-04-13

Predicting the Influence of 42CrMoS4 Variability on Cold Forming through Constitutive Modelling and Fracture Analysis

Aratz Barandiaran[1,a*], Lander Galdos[1,b], David Abedul[1,c] and Julen Agirre[1,d]

[1]Mechanics and Industrial Production Department, Mondragon Unibertsitatea, Loramendi 4, 20500 Mondragon, Spain

[a*]aratz.barandiaran@alumni.mondragon.edu, [b]lgaldos@mondragon.edu, [c]dabedul@mondragon.edu, [d]jagirreb@mondragon.edu

Keywords: cold forging, 42CrMoS4, constitutive modelling, ductile fracture.

Abstract. This work analyses the influence of batch-to-batch variability on both strain hardening and ductile fracture behaviour of a 42CrMoS4 steel under cold forging conditions. Mechanical testing combined with full-field strain measurements and finite element simulations is used to characterise material response and fracture under different stress states. Batch-dependent hardening laws are identified, and ductile fracture initiation is described using the Hosford–Coulomb criterion, calibrated independently for each material batch. The identified fracture strains and fracture response exhibit a measurable variability between batches, even for similar stress-state conditions. The results provide quantitative evidence of batch-dependent material behaviour relevant for forming simulations.

Introduction

Cold forging is widely used for the production of high-performance mechanical components, where reliable prediction of material flow, forming forces and failure is essential. Finite Element Method (FEM) simulations are routinely employed to support process design and optimization; however, their accuracy strongly depends on the proper calibration of constitutive models describing the mechanical response of the material.

Under cold forging conditions, the mechanical response of metallic materials is governed by strain hardening, while ductile fracture represents a critical failure mode that must be avoided to ensure process robustness. Plastic flow is commonly described using constitutive laws calibrated from mechanical testing [1], while stress-state dependent fracture criteria have been shown to improve failure prediction under complex loading conditions [2]. The combined effect of stress triaxiality and Lode angle parameter plays a key role in ductile fracture initiation under multiaxial stress states [3]. Consequently, hybrid experimental–numerical approaches combining mechanical testing, full-field strain measurements and FEM simulations are increasingly used to identify both hardening and fracture parameters [4].

Despite these advances, industrial simulations are typically based on a single representative material behaviour for a given steel grade [5]. However, batch-to-batch variability related to differences in chemical composition, microstructure and processing history may lead to measurable variations in mechanical response, even within the same material designation [6]. Such variability affects both the identification of strain hardening behaviour and the calibration and transferability of ductile fracture models, becoming particularly relevant in digital twin and model-based process control applications, where predictive accuracy is required despite inherent material scatter.

Ductile fracture tests generally exhibit non-proportional loading paths, with evolving stress triaxiality and Lode angle parameter during deformation. For modelling simplicity, a proportional loading assumption is commonly adopted, using mean stress-state approaches based on averaged values up to fracture for the identification of fracture initiation criteria.

This work investigates the influence of raw material variability on strain hardening and ductile fracture behaviour of a 42CrMoS4 steel. Five industrial batches were characterised through tensile and compression tests, complemented by metallographic analysis and hardness measurements, to identify batch-dependent strain hardening behaviour. The hardening laws were subsequently refined using experimental–numerical calibration based on fracture tests. Ductile fracture behaviour was

analysed using Notched (NT), Plane Strain (PS) and Shear (SH) specimens, combining experimental testing, Digital Image Correlation (DIC) and FEM simulations. Average stress triaxiality and Lode angle parameter at fracture were used to calibrate a Hosford–Coulomb fracture initiation model based on a proportional mean stress-state approach. The impact of batch-to-batch variability on fracture modelling in cold forging simulations is finally discussed.

Experimental Procedure

The investigated material was a 42CrMoS4 steel supplied as industrial cylindrical billets for cold forming, with a diameter of Ø25 mm. Five industrial batches (B1–B5), originating from different manufacturers and different heats, were analysed to assess batch-to-batch variability within the same steel grade. All batches were investigated in the as-received condition and characterised in terms of chemical composition, microstructure and hardness. The chemical composition of each batch was obtained from the corresponding material certificates and is reported in Table 1. Minor variations in alloying elements were observed among batches, which may contribute to differences in microstructure and mechanical response and support the batch-to-batch comparison discussed in the following sections.

Table 1. Chemical composition of the investigated 42CrMoS4 batches (wt.%).

	C	Mn	Si	Cr	Mo	P	S	Al
B1	0.420	0.790	0.170	0.978	0.173	0.012	0.022	0.023
B2	0.433	0.815	0.162	0.991	0.175	0.014	0.024	0.025
B3	0.433	0.752	0.181	1.130	0.169	0.010	0.026	-
B4	0.430	0.797	0.163	0.994	0.174	0.014	0.024	0.024
B5	0.420	0.750	0.200	1.060	0.174	0.011	0.026	0.022
42CrMoS4	0.427 ± 0.007	0.781 ± 0.029	0.175 ± 0.016	1.031 ± 0.064	0.173 ± 0.002	0.012 ± 0.002	0.025 ± 0.002	0.023 ± 0.001

Metallographic analyses were performed on transverse sections of the cylindrical billets to characterise the initial microstructure and identify possible differences between batches. Samples were prepared using standard grinding and polishing procedures up to 1 µm and etched with Nital. Optical microscopy observations were conducted at the same magnification for all batches to allow a consistent comparison of grain morphology and phase distribution. Representative micrographs are shown in Fig. 3.

Vickers micro-hardness measurements were performed on the same transverse sections to evaluate hardness distributions and batch-to-batch variability. Prior to testing, the specimen surfaces were prepared following standard metallographic procedures, with a final polishing step using a 1 µm diamond suspension. Measurements were carried out using a Vickers micro-hardness tester (Qness Q60 A+ EVO) with an applied load of 0.5 kgf (HV0.5) and a dwell time of 12 s. Multiple indentations were performed along a diagonal path across the section, as illustrated in Fig. 4(b).

Mechanical testing was conducted to characterise both strain hardening and fracture behaviour. All specimens were manufactured by wire electro-discharge machining (EDM). Uniaxial tension (Fig. 1 (a)) and uniaxial compression (Fig. 1 (b)) tests were used to identify the hardening response, while NT (Fig. 1 (c)), PS (Fig. 1 (d)) and SH (Fig. 1 (e)) specimens were employed to investigate fracture under different stress states. Uniaxial tension tests were performed on standard flat specimens with a gauge width of 6 mm and a thickness of 1.5 mm, following ASTM E8/E8M-04 recommendations [7], under strain-controlled conditions at a nominal strain rate of 0.002 s^{-1}. Uniaxial compression tests were carried out under comparable quasi-static conditions, following the guidelines of ASTM E9 [8], to extend the hardening characterisation to higher plastic strain levels.

Fracture tests were conducted under displacement control at a constant crosshead speed of 0.015 mm/s. Extensometers with gauge lengths of 60 mm and 15 mm were used to measure global

displacement for the NT and PS/SH specimens, respectively (blue dots in Fig. 1). The geometries of all the tested specimens are shown in Fig. 1. Force and displacement were continuously recorded during the tests. At least three repetitions were performed for each specimen geometry to ensure repeatability, except for the uniaxial tension tests, for which only two repetitions were conducted due to limited material availability.

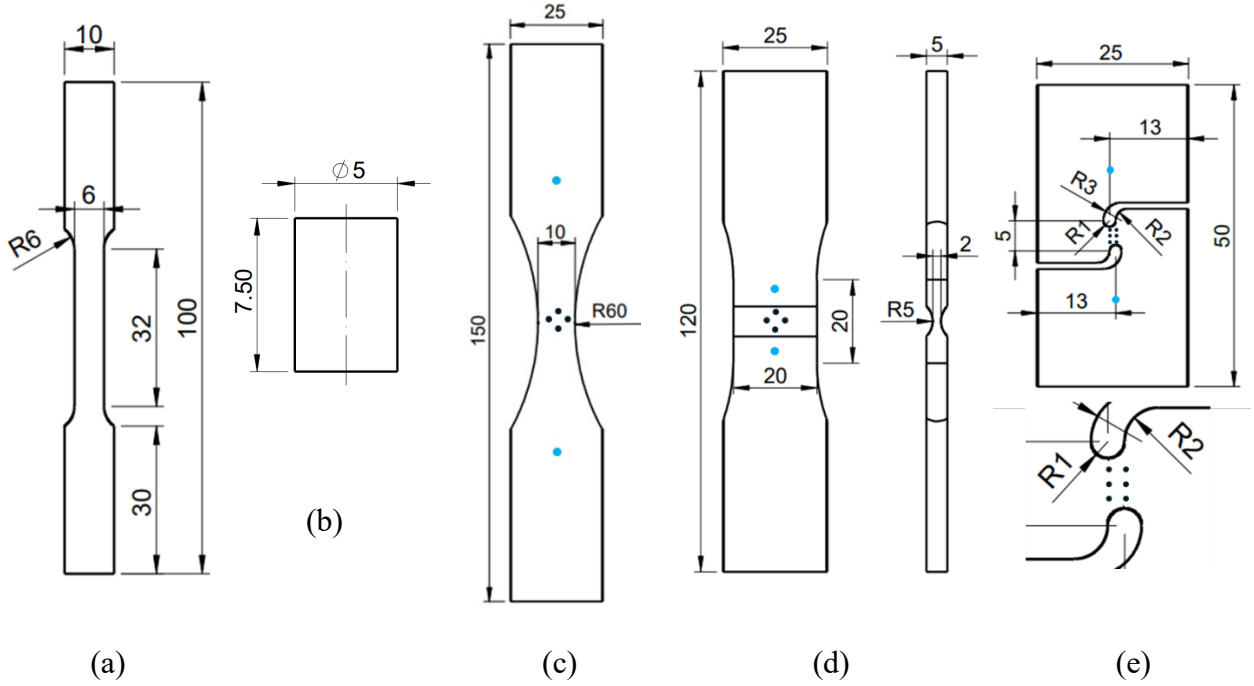

Fig. 1. Specimen geometries used for mechanical testing: (a) Uniaxial tension, (b) Uniaxial compression, (c) NT, (d) PS and (e) SH.

Force measurements were directly acquired from a Universal Testing Machine (UTM) equipped with a 100 kN load cell and recorded through a National Instruments USB-6001 data acquisition system. The force signal was sampled at a frequency six times higher than that used for DIC image acquisition.

Full-field displacement and strain measurements were obtained by DIC. Specimen surfaces were prepared with a random black speckle pattern on a white background. Images were acquired using a JAI GO-5000M-USB CCD camera (2560 × 2048 pixels) and processed with GOM Correlate 2019 to compute displacement and strain fields up to fracture (see Fig. 2(a)). The acquisition frequency was adjusted for each specimen geometry to record approximately 500 images per test, resulting in sampling rates of 2 Hz, 5 Hz and 3 Hz for the NT, PS and SH tests, respectively. Local strains were monitored using virtual extensometers (black dots in Fig. 1) with a gauge length of 5 mm for the NT and PS specimens, while three local extensometers with a gauge length of 1 mm were used for the SH specimens to track local deformation and rotation.

For uniaxial tension tests, the extensometer signal was used to determine the macroscopic strain within the gauge length following ASTM E8/E8M-04 recommendations. Experimental data were converted into true stress–true strain curves and used, together with uniaxial compression tests, for the identification of batch-dependent strain hardening behaviour.

Fracture initiation was defined as the onset of the first visible crack, associated with a sudden drop in the recorded force, and was consistently used to define the reference fracture point for all specimen geometries. Post-mortem fractographic analyses were performed on fractured specimens from a representative batch (B1) to qualitatively assess fracture mechanisms associated with the different specimen geometries and stress states. Fracture surfaces were examined using a Scanning Electron Microscope (SEM), FEI Nova NanoSEM 450, following established approaches reported in the literature [9]. These experimental results constitute the basis for the numerical analyses and fracture modelling presented in the following sections.

Experimental Results

The strain hardening behaviour of the five batches was identified from uniaxial tension and uniaxial compression tests, combined using a plastic work equivalence approach to extend the strain range [10], and fitted with the simplified Hensel–Spittel constitutive law [11]. Fig. 2(b) compares the fitted true stress–true strain curves for each batch, showing a similar overall hardening trend but noticeable differences in flow stress level and hardening response between batches.

To quantify the observed variability, selected mechanical properties were extracted for each batch and are summarised in Table 2. Yield strength (YS), ultimate tensile strength (UTS) and elongation at fracture (A%) were obtained from uniaxial tension tests while average hardness values (HV0.5) were derived from micro-hardness measurements. In addition, true stress values at $\varepsilon = 0.4$ and $\varepsilon = 0.8$ were extracted from the fitted hardening curves as representative points of the medium and high plastic strain regimes relevant for subsequent fracture modelling, as indicated in Fig. 2(b). The last row of Table 2 reports the average value of each property across the five batches. The simplified Hensel-Spittel constitutive law is expressed as Eq. 1:

$$\sigma = A_1 \, (\varepsilon + \varepsilon_{b0})^{m_2}. \tag{1}$$

where σ is the equivalent flow stress, ε is the equivalent plastic strain, A_1 and m_2 are material parameters, and ε_{b0} is a reference plastic strain representing the initial hardening state of the material and avoiding singular behaviour at zero plastic strain. The parameters of the hardening law were identified separately for each batch through an inverse fitting procedure based on the combined uniaxial tension and compression data.

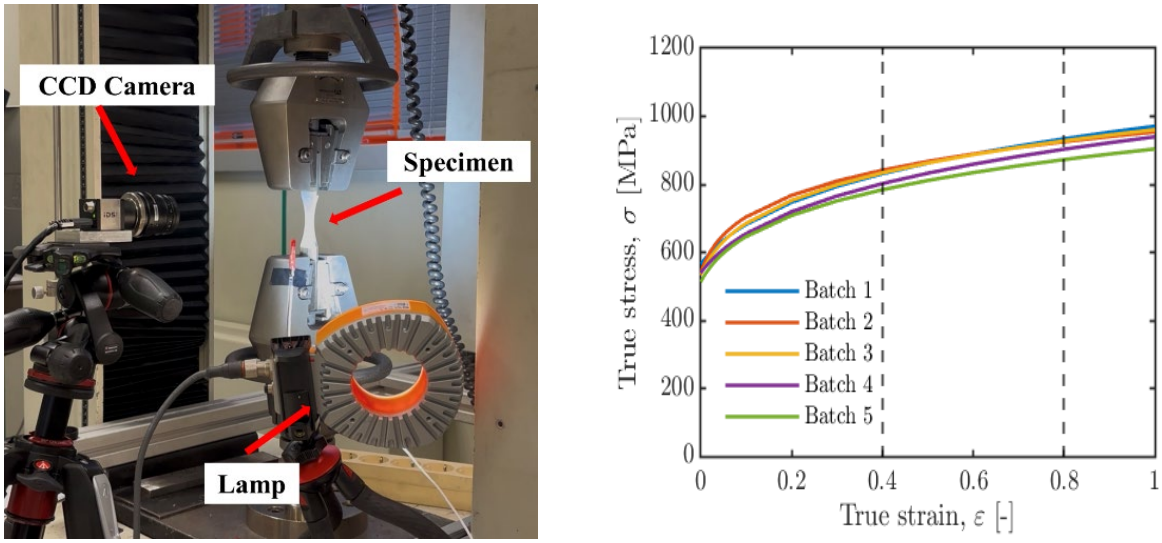

(a) (b)

Fig. 2. (a) Setup for the experimental fracture tests (b) Comparison of fitted true stress–true strain hardening curves for the investigated 42CrMoS4 batches.

Metallographic analyses were performed on transverse sections of the five batches to qualitatively assess microstructural differences. Representative optical micrographs are shown in Fig. 3. All batches were supplied in the annealed condition and exhibit a ferritic–pearlitic microstructure at the investigated magnification. Minor variations in pearlite distribution and colony arrangement were observed between batches; however, no pronounced microstructural features were identified that could alone explain the differences in strain hardening behaviour. This indicates that the observed mechanical variability is likely associated with combined effects of microstructure and processing history.

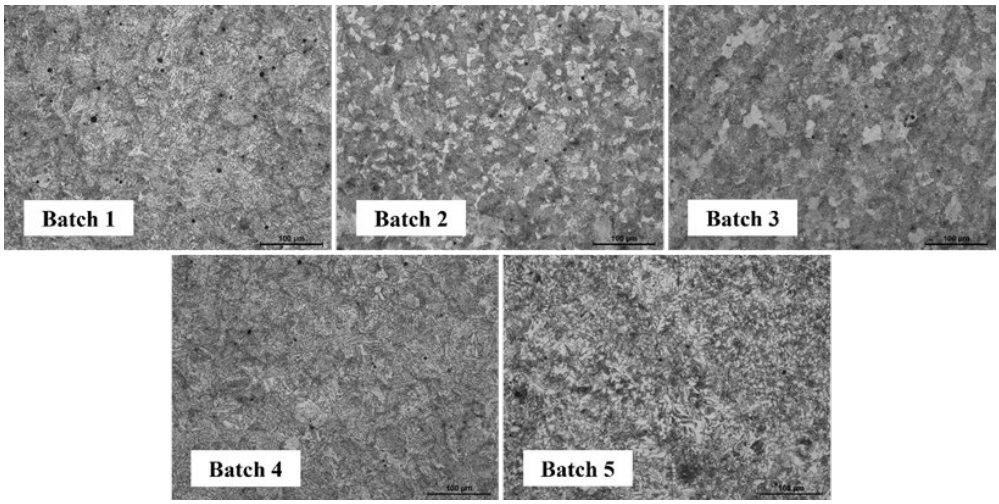

Fig. 3. Optical micrographs showing the transversal microstructure of the different 42CrMoS4 batches, acquired at the same magnification.

Vickers micro-hardness measurements (HV0.5) were performed on transverse sections of all batches. Hardness profiles obtained across the section are shown in Fig. 4(a), together with the indentation layout illustrated in Fig. 4(b). For each batch, multiple indentations were carried out along a diagonal path across the section to obtain representative hardness distributions. The measured hardness profiles exhibit a similar overall trend for all batches, with average values close to 200 HV0.5 and limited scatter, indicating a relatively homogeneous material condition at the investigated scale. No pronounced hardness gradients were observed across the section. Average hardness values for each batch are reported in Table 2. Although hardness measurements alone cannot fully explain the differences observed in the fitted strain hardening behaviour, the experimental data show an approximately linear correlation between hardness and the ultimate tensile strength (UTS). This indicates that the base hardness of the material is related to the observed variations in the strain hardening response, although the overall differences remain relatively limited.

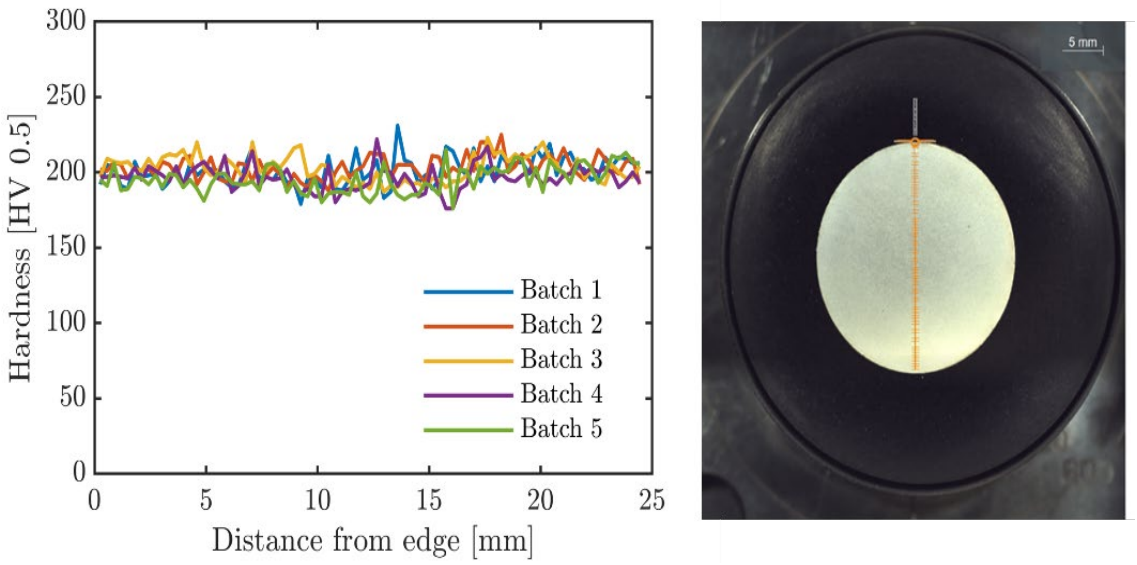

(a) (b)

Fig. 4. (a) Vickers micro-hardness (HV0.5) profiles measured across the transversal section of the investigated batches. (b) Representative indentation layout adopted for the micro-hardness measurements.

Table 2. Quantification of batch-to-batch variability based on tensile properties, micro-hardness and fitted hardening parameters for 42CrMoS4.

	YS [MPa]	UTS [MPa]	A% [-]	HV 0.5 avg	σ (ε = 0.4) [MPa]	σ (ε = 0.8) [MPa]
B1*	540 ± 0.0	598 ± 0.0	22.6 ± 0.0	200 ± 7.6	831	934
B2	491 ± 5.6	619 ± 0.8	26.6 ± 3.7	203 ± 7.5	842	925
B3	487 ± 6.2	603 ± 1.0	25.6 ± 0.8	202 ± 8.6	834	928
B4	512 ± 0.9	578 ± 1.8	23.7 ± 0.2	196 ± 8.3	802	903
B5	484 ± 9.9	570 ± 3.4	26.2 ± 0.0	195 ± 8.9	784	873
42CrMoS4	503 ± 24.0	593 ± 19.7	24.9 ± 1.7	199 ± 3.2	818.6 ± 23.4	912.6 ± 25.9

*Uniaxial tension results are based on a single valid experimental test.

Fractographic analyses were performed on fractured specimens from a representative batch (B1) to qualitatively assess fracture mechanisms under different stress states imposed by the NT, PS and SH geometries. Observations were conducted by SEM at a magnification of 6500×. Representative fractographic images are shown in Fig. 5.

For the NT specimens (Fig. 5(a)), the fracture surface exhibits a ductile morphology dominated by equiaxed dimples, indicating void nucleation, growth and coalescence under a tension-dominated stress state with elevated triaxiality. PS specimens (Fig. 5(b)) show a similar ductile mechanism; however, the dimples appear more elongated and preferentially oriented, reflecting the constrained plastic deformation associated with plane strain conditions.

In contrast, the fracture surface of the SH specimens (Fig. 5(c)) is characterized by flat facets and localized shear features, with limited evidence of void growth. This morphology indicates a shear-dominated fracture mechanism, distinctly different from the tension-driven cases. Overall, these observations highlight the strong influence of the stress state on fracture mechanisms and are consistent with the stress-state dependent fracture behaviour identified in the numerical analysis.

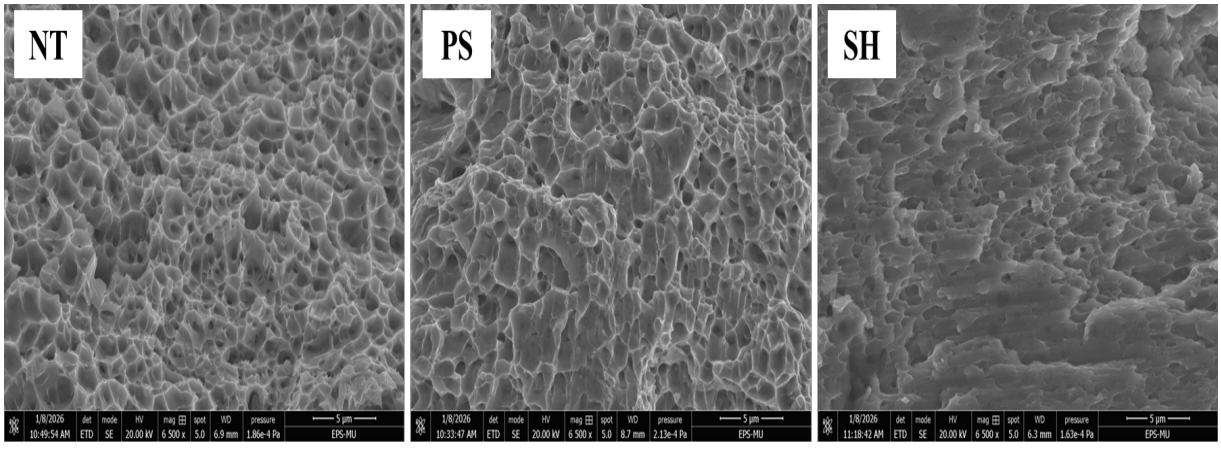

(a) (b) (c)

Fig. 5. SEM images of the fracture surfaces of (a) NT, (b) PS and (c) SH specimens, acquired at a magnification of 6500x.

Numerical Results

Based on the experimental observations, finite element simulations were performed to reproduce the fracture tests and determine the fracture strain under different loading conditions. All experimentally investigated NT, PS and SH specimen geometries were simulated for the different material batches. The simulations served to validate and, where necessary, refine the previously identified hardening model, and to provide a numerical framework for extracting the stress-state variables required for fracture analysis.

The simulations were carried out using the commercial software FORGE NxT 4.1. Geometric symmetries were exploited to reduce computational cost, with one-eighth of the geometry modelled for the NT and PS specimens and one-half for the SH specimens. The meshes consisted of linear tetrahedral elements with an enriched velocity field, using a characteristic element size of 0.1 mm in the region of interest. This mesh density was selected to ensure an adequate description of strain localization prior to fracture (see Fig. 6.).

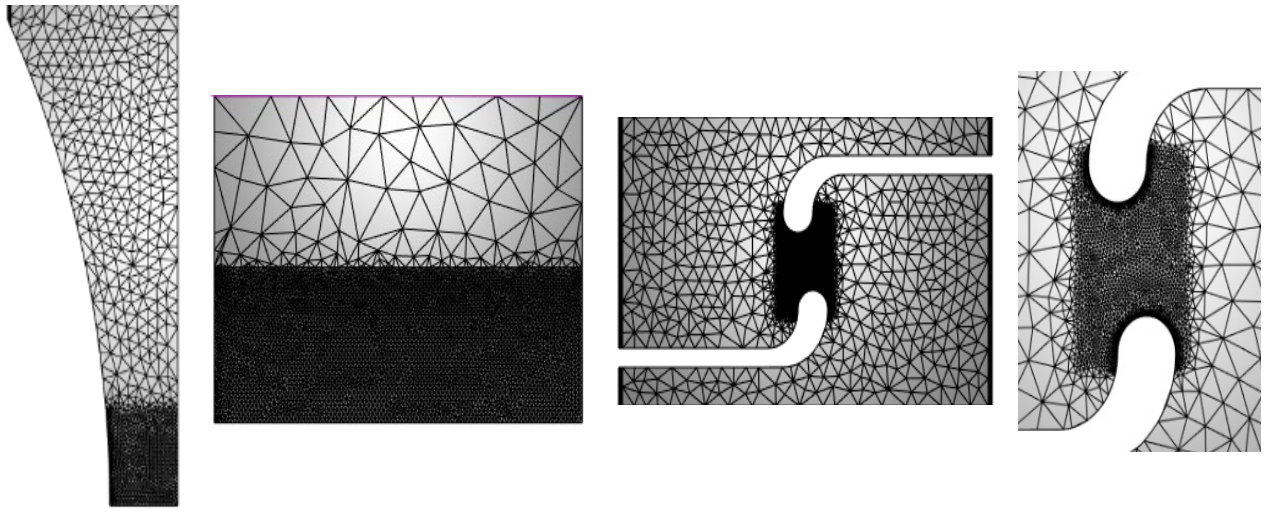

(a) (b) (c) (d)

Fig. 6. Finite element meshes used for the numerical simulations of the fracture test geometries: (a) NT specimen, (b) PS specimen, (c) SH specimen and (d) detailed view of the SH specimen showing the locally refined mesh in the fracture region with an element size of 0.1 mm.

Material behaviour was described using batch-dependent hardening laws identified from uniaxial tension and uniaxial compression tests and modelled with the simplified Hensel–Spittel constitutive law. The initial parameters were obtained by combining data from both tests through a plastic work equivalence approach and subsequently refined by calibrating numerical simulations against the experimental force–displacement response of the NT specimens.

The NT geometry was selected for this calibration due to its stable fracture behaviour and intermediate stress state. Parameter optimisation was performed independently for each batch by minimising the discrepancy between experimental and simulated force–displacement curves using the objective function defined in Eq. 2. The resulting optimised hardening parameters are summarised in Table 3.

$$X_h = \sqrt{\sum(F_{exp} - F_{sim})^2}. \quad (2)$$

where X_h represents the minimized error, F_{exp} is the experimentally measured force, and F_{sim} is the force predicted by FEM. The optimization procedure was carried out independently for each batch.

Table 3. Optimized parameters of the Hensel–Spittel hardening law identified for the five batches.

	A_1	m_2	ε_{bo}		A_1	m_2	ε_{bo}
B1	864.8	0.1848	0.05661	B4	837.1	0.1877	0.05509
B2	856.6	0.1411	0.01842	B5	854.4	0.1631	0.03187
B3	860.9	0.1611	0.02675				

To verify the calibration of the batch-dependent material models, numerical simulations of the NT, PS and SH specimens were compared with the corresponding experimental results. Model accuracy was assessed by comparing global force–displacement with the experimental measurements.

Local strain measurements were obtained from DIC by defining two virtual extensometers aligned with the Loading Direction (LD) and the Transverse Direction (TD). In the case of the SH specimens, three local virtual extensometers with a gauge length of 1 mm were used to monitor the rotation and local deformation during the test.

A representative comparison between experimental and numerical force–displacement curves and local strain measurements for the NT, PS and SH specimens is provided in Fig. 7. The comparisons correspond to the NT geometry for batch 3 (NT3), the PS geometry for batch 1 (PS1), and the SH geometry for batch 5 (SH5), selected as representative cases. This verification step ensured that the numerical model reproduces the experimentally observed mechanical response up to fracture for the different specimen geometries and batches.

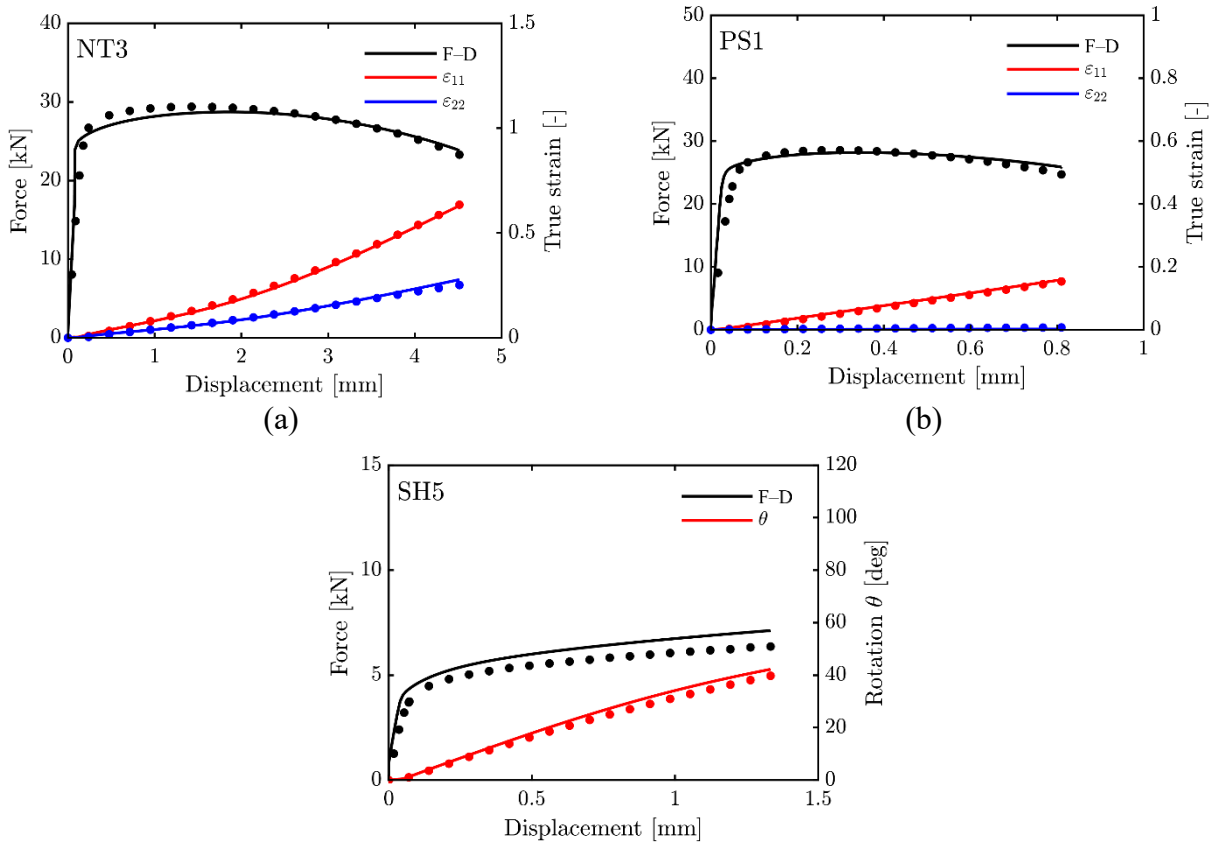

Fig. 7. Comparison of force-displacement curves and local extensometer measurements obtained experimentally (dots) and numerically (lines) for (a) NT3, (b) PS1, (c) SH5 specimens.

Fig. 8 presents the true strain fields in the LD, in the TD, as well as the equivalent strain ($\varepsilon_{eq} = \sqrt{2/3\ d^p : d^p}$), obtained from the DIC analysis at the moment of fracture for the NT, PS and SH specimens of the B2. These measurements provide valuable information regarding strain localization and the fracture initiation zones. For the NT and PS specimens (see Fig. 8 (a,b,c)), strain localization is observed at the centre of the specimen neck. The corresponding DIC results show that, in the PS specimen, the strain in the TD (see Fig. 8 (c)) is negligible when compared to the strain in the loading direction LD (see Fig. 8 (b)), confirming that the fracture initiation zone is subjected to plane strain conditions. In contrast, the DIC measurements obtained for the SH specimens indicate that strain localization occurs in the region covered by virtual extensometers, leading to peak strain values close to the specimen edge, as shown in Fig. 8 (c).

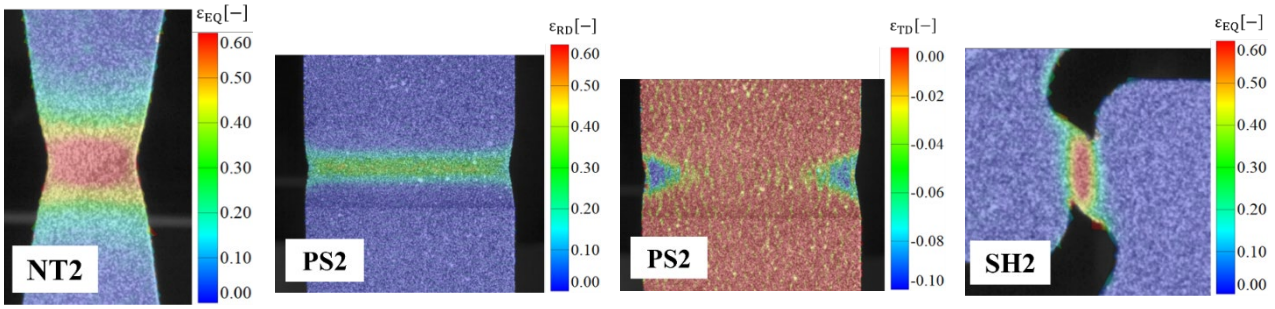

(a) (b) (c) (d)

Fig. 8. Digital image correlation (DIC) analysis at the onset of fracture, showing equivalent strain contours for the (a) NT2 and (c) SH2 specimens and (b) LD and (d) TD strain distributions for the PS2 specimen.

The initiation of ductile fracture is strongly influenced by the stress state experienced by the material during deformation. For isotropic materials, the stress state can be conveniently described in terms of the stress triaxiality, η, and the Lode angle parameter, $\bar{\theta}$, which account for the effects of hydrostatic stress and the third invariant of the deviatoric stress tensor, respectively.

The stress triaxiality is defined as the ratio between the mean stress and the von Mises equivalent stress (Eq. 3), where $\sigma_m = \frac{1}{3}\,\mathrm{tr}(\sigma)$ is the mean (hydrostatic) stress and σ_{eq} is the von Mises equivalent stress. The influence of the third invariant of the stress tensor is described by the normalized Lode angle parameter $\bar{\theta}$, defined in Eq. 4, where s is the deviatoric stress-tensor.

$$\eta = \frac{\sigma_m}{\sigma_{eq}}. \tag{3}$$

$$\bar{\theta} = 1 - \left(\frac{2}{\pi}\right)\mathrm{acos}\left(\frac{27}{2}\frac{\det(s)}{\sigma_{eq}^3}\right). \tag{4}$$

In the present work, ductile fracture initiation was modelled using the Hosford–Coulomb (HC) fracture criterion, which describes the fracture strain as a function of stress triaxiality and Lode angle parameter. This model was originally proposed by Mohr and Marcadet [4] and has been shown to accurately capture ductile fracture over a wide range of stress states. According to the HC formulation, fracture initiation occurs when the accumulated equivalent plastic strain reaches a critical value ε_f, given by Eq. 5:

$$\varepsilon_f^{HC}(\eta,\bar{\theta}) = b\left(\frac{1+c}{\left(\left[\frac{1}{2}\left(|f_1-f_2|^m+|f_2-f_3|^m+|f_3-f_1|^m\right)\right]^{\frac{1}{m}}+c\,(2\eta+f_1+f_3)\right)}\right)^{\frac{1}{a}}. \tag{5}$$

where a, b, c and m are material parameters, and the functions f_i depend on the Lode angle parameter according to Eqs. 6-8:

$$f_1(\bar{\theta}) = \frac{2}{3}\cos\left[\frac{\pi}{6}(1 - \bar{\theta})\right]. \quad (6)$$

$$f_2(\bar{\theta}) = \frac{2}{3}\cos\left[\frac{\pi}{6}(3 + \bar{\theta})\right]. \quad (7)$$

$$f_3(\bar{\theta}) = -\frac{2}{3}\cos\left[\frac{\pi}{6}(1 + \bar{\theta})\right]. \quad (8)$$

During the fracture tests investigated in this study, the stress state evolves with deformation but remains approximately proportional. For modelling simplicity, fracture modelling was performed using a mean stress-state approach, in which average values of stress triaxiality and Lode angle parameter were computed over the deformation history up to the experimentally observed fracture point. These averaged values were subsequently used for the identification of the HC model parameters.

Fig. 9 shows the evolution of the equivalent plastic strain at fracture as a function of the stress triaxiality η and the Lode angle parameter $\bar{\theta}$ for the different specimen geometries from batch B1. The stress triaxiality and Lode angle parameter were evaluated at the material point experiencing the maximum equivalent plastic strain at the instant where fracture takes place, which is assumed to represent the fracture initiation location according to ductile fracture theory. In addition, the fracture strain predicted by the calibrated HC model, ε_f^{HC}, is reported at the corresponding stress-state values for each geometry. PS specimens exhibit the highest stress triaxiality values, whereas NT specimens show intermediate triaxiality levels, and SH specimens are characterised by near-zero triaxiality, indicative of shear-dominated conditions. Regarding the Lode angle parameter, NT specimens present clearly positive $\bar{\theta}$ values, while PS and SH specimens show $\bar{\theta}$ values close to zero.

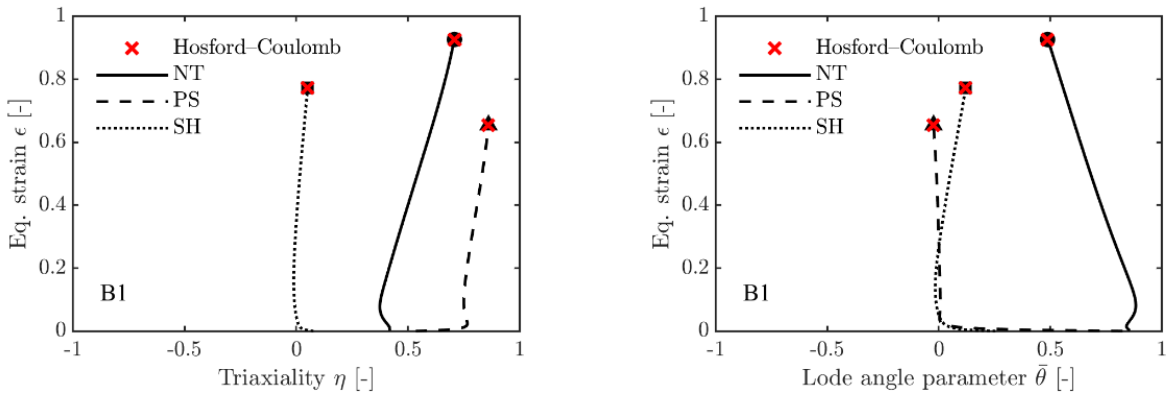

Fig. 9. Stress-state-dependent fracture strain and Hosford–Coulomb predictions for batch B1: (a) fracture strain vs stress triaxiality; (b) fracture strain vs Lode angle parameter.

Fig. 10 compares the equivalent plastic strain at fracture as a function of the mean stress triaxiality η and the mean Lode angle parameter $\bar{\theta}$ for the different batches and specimen geometries. For a given geometry, noticeable differences in fracture strain are observed between batches, despite relatively similar mean stress-state parameters. In the NT configuration, the batches exhibit comparable η (Fig. 10 (a)) and $\bar{\theta}$ values (Fig. 10 (d)), while the fracture strain shows a clear batch-dependent scatter. A similar trend is observed for the PS specimens, where variations in fracture strain occur at nearly constant η (Fig. 10 (b)) and slightly varying $\bar{\theta}$ (Fig. 10 (e)). In the SH configuration, differences in fracture strain between batches are also evident, even though the mean triaxiality remains close to zero (Fig. 10 (c)) and the Lode angle parameter varies within a narrow range (Fig. 10 (f)).

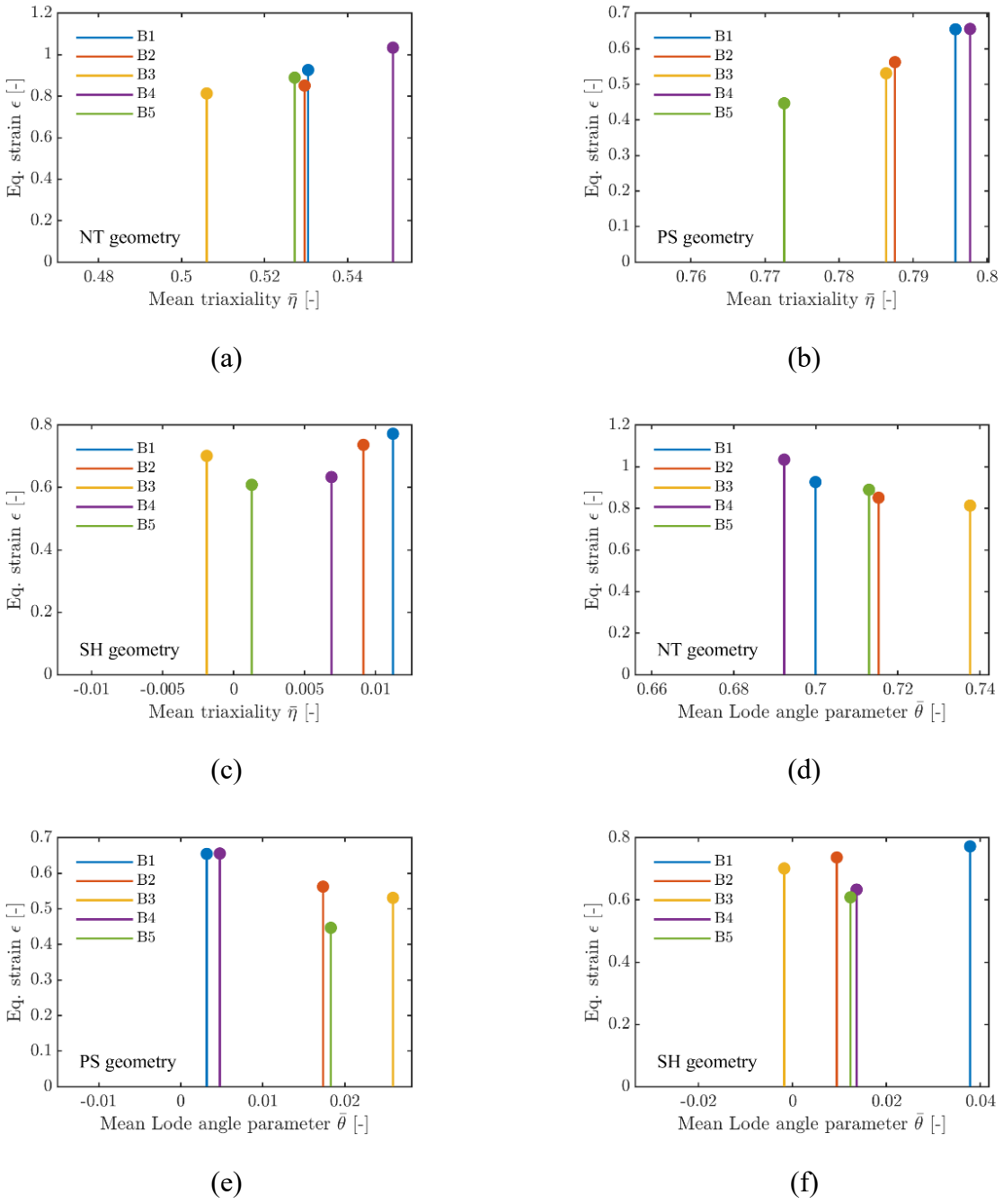

Fig. 10. Comparison between batches in terms of mean stress triaxiality $\bar{\eta}$ for (a) NT, (b) PS and (c) SH specimen geometries and in terms of mean Lode angle parameter $\bar{\theta}$ for (d) NT, (e) PS and (f) SH specimen geometries.

Fig. 11 (a) shows the HC fracture surface obtained for Batch B1, represented in the η, $\bar{\theta}$ space. The surface illustrates the stress-state dependency of the predicted equivalent fracture strain, with higher fracture strains associated with low triaxiality and shear-dominated stress states, and a progressive reduction of ductility with increasing stress triaxiality [12]. The experimentally observed fracture points corresponding to the NT, PS and SH specimen geometries are also indicated, showing a consistent alignment with the predicted fracture surface.

Fig. 11 (b) shows the plane stress fracture loci predicted by the HC model for the five investigated batches, calibrated using NT, PS and SH experimental data. The curves display a consistent qualitative dependence of fracture strain on stress triaxiality, while exhibiting batch-dependent offsets across the investigated range.

Comparable scatter is observed in the regions of triaxiality associated with the stress states employed for model calibration, indicating that batch-to-batch variability is preserved under the stress conditions governing the fitting of the fracture model.

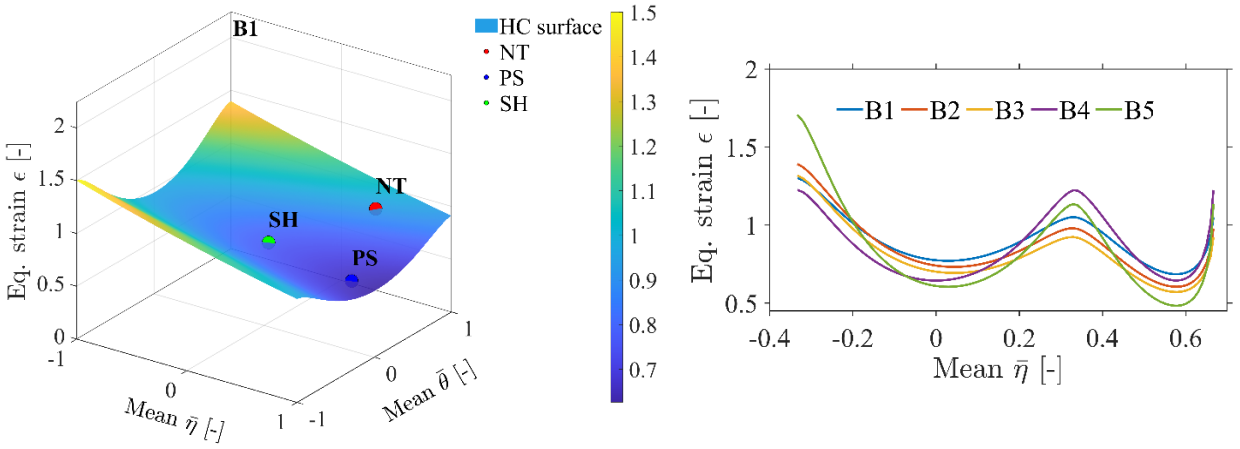

(a) (b)

Fig. 11. (a) HC fracture surface obtained for the representative Batch B1, with the experimental fracture points corresponding to NT, PS and SH geometries. (b) Batch-dependent plane stress fracture loci predicted by the HC model.

For completeness, the optimized HC model parameters identified independently for each material batch are summarized in Table 4. The reported parameters correspond to the best-fit values obtained under the assumption of proportional loading. The observed batch-to-batch variability in the parameter values is consistent with the differences in fracture response highlighted by the plane stress fracture loci.

Table 4. Batch-dependent HC model parameters identified under proportional loading.

	a	b	c	n		a	b	c	n
B1	1.9215	1.0506	0.000969	0.009069	B4	1.8522	1.2247	0	0.011828
B2	1.9276	0.9785	0.001321	0.007519	B5	1.7970	1.1339	0.00274	0.013452
B3	1.9221	0.9220	0.001462	0.008190					

Conclusion

Based on the experimental and numerical analyses performed in this study, the main conclusions can be summarised as follows:

- Batch-to-batch variability leads to significant differences in both strain hardening and ductile fracture behaviour, even for materials sharing the same nominal steel grade.
- The hybrid experimental–numerical approach enabled the identification of batch-dependent material behaviour, which was consistently captured by independently calibrating the simplified Hensel–Spittel constitutive law and the Hosford–Coulomb fracture criterion for each batch.
- Although comparable mean stress states were obtained for a given specimen geometry, a noticeable scatter in fracture strain and, therefore, in the resulting fracture response was observed between batches.
- This scatter tends to be more pronounced under tension-dominated loading conditions, whereas reduced variability is generally observed for shear-dominated stress states.
- The assumption of a single representative material behaviour may therefore introduce non-negligible uncertainties in fracture predictions.

- The proposed methodology provides a practical framework to quantify material variability and supports the development of more reliable numerical simulations and digital twin approaches for cold forging applications.

Acknowledgement

The authors gratefully acknowledge Jesús Oñate S.A. for providing the material and for his technical support. Financial support from the Gipuzkoako Foru Aldundia within the framework of the FORBIL project is also acknowledged.

Bibliography

[1] J. Besson, G. Cailletaud, J.L. Chaboche, S. Forest, Non-linear Mechanics of Materials, Springer, Dordrecht, 2009.

[2] Y. Bao, T. Wierzbicki, On fracture locus in the equivalent strain and stress triaxiality space, International Journal of Mechanical Sciences 46 (2004) 81–98.

[3] Y. Bai, T. Wierzbicki, A new model of metal plasticity and fracture with pressure and Lode dependence, International Journal of Plasticity 24 (2008) 1071–1096.

[4] D. Mohr, S.J. Marcadet, Micromechanically motivated phenomenological Hosford–Coulomb model for ductile fracture, International Journal of Solids and Structures 67–68 (2015) 40–55.

[5] A.A. Benzerga, J.B. Leblond, Ductile fracture by void growth to coalescence, Advances in Applied Mechanics 44 (2010) 169–305.

[6] L. Muñiz, J. Trinidad, L. Galdos, Analysis of the Mechanical and Microstructural Fluctuations of High-Strength Steels and Their Effect on Bending Angle, Metals 10 (2020) 1–17.

[7] ASTM International, ASTM E8/E8M-04: Standard Test Methods for Tension Testing of Metallic Materials, ASTM International, West Conshohocken, PA, 2004.

[8] ASTM International, ASTM E9/E9M-09: Standard Test Methods for Compression Testing of Metallic Materials at Room Temperature, ASTM International, West Conshohocken, PA, 2009.

[9] A. Weck, D.S. Wilkinson, E. Maire, H. Toda, Experimental investigation of void coalescence in metallic sheets containing laser drilled holes, Acta Materialia 56 (2008) 2919–2932.

[10] R. Hill, The Mathematical Theory of Plasticity, Oxford University Press, Oxford, 1950.

[11] A. Hensel, T. Spittel, Kraft- und Arbeitsbedarf bildsamer Formgebungsverfahren, Deutscher Verlag für Grundstoffindustrie, Leipzig, 1978.

[12] D. Abedul, L. Galdos, E. Sáenz de Argandoña, F. Gálvez, B. Erice, Effect of the loading-rate and stress state on the constitutive modelling and fracture of 2205 Duplex stainless steel, International Journal of Impact Engineering 191 (2024) 104991.

The publication of this article was funded by the Mondragon Goi Eskola Politeknikoa, J.M.A. S.Coop